Globally defining the effects of mutations in a picornavirus capsid

Florian Mattenberger[1], Victor Latorre[1], Omer Tirosh[2], Adi Stern[2], Ron Geller[1*]

[1]Institute for Integrative Systems Biology, I[2]SysBio (Universitat de València-CSIC), C. Catedràtic José Beltrán 2, Paterna, 46980, Spain.

[2]The Shmunis School of Biomedicine and Cancer Research, Tel-Aviv University, Tel-Aviv, Israel

*Corresponding author: Ron Geller, Institute for Integrative Systems Biology, I[2]SysBio (Universitat de València-CSIC), C. Catedràtic José Beltrán 2, Paterna, 46980, Spain. Email: ron.geller@uv.es

ABSTRACT

The capsids of non-enveloped viruses are highly multimeric and multifunctional protein assemblies that protect the viral genome between infection cycles, dictate host and cell tropism, and mediate evasion of humoral immune responses. As such, capsids play key roles in viral biology and pathogenesis. Despite their importance, a comprehensive understanding of how mutations affect viral fitness across different structural and functional attributes of the capsid is lacking. To address this limitation, we globally define the effects of mutations in the capsid of a human picornavirus, generating a comprehensive dataset encompassing >90% of all possible single amino acid mutations. Moreover, we use this information to identify structural and sequence determinants that accurately predict mutational fitness effects, refine evolutionary analyses, and define the sequence specificity of key capsid encoded motifs. Finally, capitalizing on the sequence requirements identified in our dataset for capsid encoded protease cleavage sites, we implement and validate a bioinformatic approach for identifying novel host proteins targeted by viral proteases. Our findings present the most comprehensive investigation of mutational fitness effects in a picornavirus capsid to date and illuminate important aspects of viral biology, evolution, and host interactions.

Keywords: Deep mutational scanning; mutational fitness effects; capsid; picornavirus; viral protease;

INTRODUCTION

The capsids of non-enveloped viruses are among the most complex of any viral protein. These highly multimeric structures must correctly assemble around the genome from numerous subunits, at times numbering in the hundreds, while avoiding aggregation [1–3]. Moreover, the assembled structure must be both sufficiently stable to protect the viral genome during its transition between cells yet readily disassemble upon entry to initiate subsequent infections. For these functions to be achieved, viral capsids must encode the information for interacting with numerous cellular factors that are required to correctly fold and assemble around the genome [4–8]. Viral capsids also play key roles in pathogenesis, dictating host and cell tropism by encoding the determinants for binding cellular receptors [9,10] and mediating escape from humoral immune responses [11,12]. As a result, viral capsids show the highest evolutionary rates among viral proteins.

The picornaviruses constitute a large group of single-stranded, positive-sense RNA viruses and include several pathogens of significant medical and economic impact [13]. Their relative simplicity and ease of culture have made picornaviruses important models for understanding virus biology. Among the many breakthroughs achieved with these viruses was the determination of the first high-resolution structure of the capsid of an animal virus, making the picornavirus capsid the prototypical non-enveloped, icosahedral viral capsid [13]. Picornavirus capsid genesis initiates with the co-translational release of the P1 capsid precursor protein from the viral polyprotein via the proteolytic activity of the viral encoded 2A protease [7,13]. Subsequently, the viral encoded 3CD protease ($3CD^{pro}$) cleaves the P1 capsid precursor to liberate three capsid proteins (VP0, VP3, and VP1), generating the capsid protomer. Five protomers then assemble to form the pentamer, twelve of which assemble around the viral genome to yield the virion. Finally, in some picornaviruses, VP0 is further cleaved into two subunits, VP4 and VP2, following genomic

encapsidation to generate the infectious, 240 subunit particle [7,13]. Work over the years has identified numerous host factors that help support capsid formation [4,5,14–16], defined antibody neutralization sites [11], and identified numerous host receptors for many members of this viral family [9].

Despite significant progress in understanding the structure and function of picornavirus capsids, a comprehensive understanding of how mutations affect viral fitness across different structural and functional attributes is lacking. To address this, we perform a comprehensive analysis of mutational fitness effects (MFE) across the complete capsid region of the human picornavirus coxsackievirus B3 (CVB3), analyzing >90% of all possible single amino acid mutations. Furthermore, using this data, we develop models to predict the effect of mutations with high accuracy from available sequence and structural information, improve evolutionary analyses of CVB3, and define the sequence preferences of several viral encoded motifs. Finally, we use the information obtained in our dataset for the sequence requirements of capsid encoded 3CD protease cleavage sites to identify host targets of this viral protease. Overall, our data comprise the most comprehensive survey of MFE effects in a picornavirus capsid to date and provide important insights into virus biology, evolution, and interaction with the host.

RESULTS

Deep mutational scanning of a CVB3 capsid

To generate CVB3 libraries encoding a large amount of diversity in the capsid region, we used a codon-level PCR mutagenesis method [17]. The mutagenesis protocol was performed on the capsid precursor region P1 in triplicate to generate three independent mutagenized libraries (Mut Library 1-3; Fig. 1A). From these, three independent viral populations (Mut Virus 1-3) were derived by electroporation of in vitro transcribed viral RNA into HeLa-H1 cells (Fig. 1A). High-fidelity next-generation sequencing [18] was then used to analyze the mutagenized libraries and resulting viruses, unmutagenized virus populations (WT virus 1-2), as well as controls for errors occurring during PCR (PCR) and reverse transcription (RT-PCR). High coverage was obtained for all samples (>10^6 per codon across all experimental conditions and >$6.5x10^5$ for the controls; Supplementary Table S2). Due to the high rate of single mutations within codons observed in the RT-PCR control compared to the mutagenized virus populations (Supplementary Table S2), all single mutants were omitted from our analysis to increase the signal-to-noise ratio. While this resulted in an inability to analyze 83.4% of synonymous codons in the capsid region (1746/2094) only 2.8% of non-synonymous mutations were lost to analysis (458/16,169). Upon removing single mutations within codons, we obtained a large signal-to-noise ratio in the average mutation rate of 510x (range 449–572) and 245x (range 174–285) for the mutagenized libraries and viruses, respectively, compared to their error controls (Fig. 1B and Supplementary Table S2). On average, 0.9 (range 0.8–1.02) codon mutations were observed per genome, which was in agreement with Sanger sequencing of 59 clones (range 18–23 per library; Fig. S1 and Supplementary Table S3). As expected, the rate of stop codons, which should be invariably lethal in the CVB3 capsid, decreased significantly following growth in cells to <0.5% of that observed in the corresponding mutagenized libraries ($p < 0.005$ by paired t-test on log-transformed data; Supplementary Table S2). No major bias was observed in the position within a codon where mutations were observed (Fig. S2A) nor in the type of mutation (Fig. S2B), except for the WT virus, which had a high

rate of A to G transitions in the two independent replicates analyzed. Of all 16,169 possible amino acid mutations in the capsid region (851 AA x 19 AA mutation = 16,169), a total of 14,839 amino acid mutations were commonly observed in all three mutagenized libraries, representing a 91.8% of all possible amino acid mutations in the capsid region, allowing us to globally assess the effects of the vast majority of amino acid mutations on the capsid (Fig. 1C).

Mutational fitness effects across the CVB3 capsid

We next derived the mutational fitness effects (MFE) of each observed mutation by examining how its frequency changed relative to that of the WT sequence following growth in cells. The preferences for the different amino acids at each position (amino acid preferences [19]) showed a high correlation between biological replicates (Spearman's $\rho > 0.83$; Supplementary Figure S3 and Supplementary Table S4 MFE). Overall, most mutations in the capsid were deleterious, with only 1.2% of mutations increasing fitness relative to the WT amino acid (Fig. 2A and Supplementary Table S4). Hotspots where mutations were tolerated were observed at several regions across the capsid (Fig. 2A). These hotspots largely overlapped with highly variable regions in natural sequences, as measured by Shannon entropy in the enterovirus B family, indicating that lab measured MFE reflect natural evolutionary processes (Fig. 2A, top). Indeed, a strong correlation was observed between MFE and sequence variability for the enterovirus B genus (Spearman's $\rho = 0.59$, $p < 10^{-16}$; Fig. 2B). Similarly, antibody neutralization sites overlapped with hotspots for mutations (Fig. 2A, top) and were significantly less sensitive to mutations ($p < 10^{-16}$ by Mann-Whitney test; Fig. 2C). As expected, mutations were also less deleterious in loops compared to β-strands ($p < 10^{-16}$ by Kruskal-Wallis test; Fig. 2D), at surface residues compared to core residues ($p < 10^{-16}$ by Kruskal-Wallis test; Fig. 2E), and for mutations predicted to be destabilizing ($p < 10^{-16}$ by Mann-Whitney test; Fig. 2F) or aggregation-prone ($p < 10^{-16}$ by Mann-Whitney test; Fig. 2G). Importantly, independent validation of the

MFE of 10 different mutants using a sensitive qPCR method [20] showed a strong correlation with the DMS results (Spearman's $\rho = 0.9$, $p < 0.001$; Supplementary Table S5).

Prediction of MFE from available structural and sequence information

As MFE correlated with natural sequence variation and different structural features of the capsid (Fig. 2), we next investigated if MFE could be predicted from available structural and sequence information. For this, we obtained a dataset of 52 parameters, including structural information derived from the crystal structure of the CVB3 capsid (PDB:4GB3), amino acid properties, natural variation in available enterovirus sequences (Shannon entropy), and predicted the effects of mutation on stability and aggregation propensity using FoldX [21] and TANGO [22], respectively (Supplementary Table S6). We then employed a random forest algorithm to identify the parameters that can best predict MFE, limiting our analysis to sites that present in the crystal structure and where mutations were observed in at least 2 replicates to improve accuracy (total of 9,685 mutations). Overall, a model trained on 70% of the dataset was able to predict the remaining 30% of the data (2,905 mutations) with high accuracy (Spearman's $\rho > 0.75$, Pearson's $r = 0.76$; $p < 10^{-16}$; Fig. S4A,B). Surprisingly, a random forest model trained on the top five predictors alone showed similar accuracy (Spearman's $\rho = 0.73$, Pearson's $r = 0.73$; $p < 10^{-16}$; Fig. 3B). Excluding natural sequence variation, amino acid identity, or structural attributes reduced model predictability significantly (>20%; data not shown), suggesting a combination of evolutionary, sequence, and structural information best explains MFE. Using an alternative approach, we were able to predict the data with slightly lower accuracy using a linear model with the same five predictors ($p < 10^{-16}$, Spearman's $\rho = 0.67$, Pearson's $r = 0.67$; Fig. S4C). Together, these results suggest that the prediction of MFE in the CVB3 capsid can be achieved at relatively high accuracy based on available structural and sequence information. Due to the high conservation of capsid structure in picornaviruses, as well as the availability

of numerous capsid sequences and structures, these findings are likely generalizable to related picornaviruses.

Experimentally measured MFE inform of natural evolutionary processes

We next examined if our experimentally measured MFE could improve phylogenetic models of CVB3 evolution by incorporating site-specific amino acid preferences using PhyDMS [23]. Indeed, significant improvement in model fit was observed (Table 1 PHY; $p < 10^{-16}$ using a log-likelihood test compared to non-site-specific codon models), supporting the relevance of our results to understanding evolutionary processes in nature. Nevertheless, selection in nature was significantly more stringent than in the lab ($\beta = 2.18$), indicating the presence of additional selection pressures. As laboratory conditions lack selection from antibodies, we used the sum of the absolute differential selection observed at each site [24] to examine whether known antibody neutralization sites show differential selection between the two environments (Supplementary Table S7). Indeed, antibody neutralization sites showed significantly higher differential selection values compared to other residues ($p < 10^{-6}$ by Mann-Whitney test; Fig. 4A). Moreover, the three sites showing the strongest overall differential selection were found in known antibody neutralization sites: position 226 and 242 in the EF loop (residues 157 and 173 of VP2) and position 650 in the BC loop (residue 80 of VP1; Fig. 4B-D and Supplementary Table S7). In summary, incorporation of our experimentally derived amino acid preferences into phylogenetic analyses significantly improved model fit and identified residues in antibody neutralization sites that show differential selection, suggesting these may play important roles in immune evasion in vivo.

Insights into capsid encoded motifs: Myristoylation and protease cleavage

Picornavirus capsids undergo a complex assembly path to generate the infectious particle. These include myristoylation, cleavage by the viral proteases 2A and $3CD^{pro}$, as well as interaction with cellular chaperones and glutathione [4,7,14–16] (Fig. 5A). Having obtained a comprehensive dataset for MFE across the capsid, we next examined the sequence requirements for several of these capsid encoded motifs. Specifically, myristoylation of the N-terminal glycine is essential for virion assembly [16]. In agreement with this, the N-terminal glycine in the CVB3 capsid showed the strongest average fitness cost upon mutation in the capsid (Fig. S5 and Supplementary Table S4). The remaining sites in the myristoylation motif agreed with the canonical myristoylation motif in cellular proteins (Prosite pattern PDOC00008) [25], albeit with increased selectivity at three of the six positions (Fig. S5A). On the other hand, a conserved WCPRP motif in the C-terminal region of VP1 that was shown to be important for $3CD^{pro}$ cleavage of the related foot and mouth disease virus capsid (FDMV; YCPRP motif) [26] was found to be intolerant to mutations compared to other capsid residues ($p < 0.05$ versus all other positions by Mann-Whitney test; sites 815-819 in CVB3). Moreover, within this motif, the sites showing the highest average fitness cost in our DMS dataset were identical to analogous positions in FMDV that resulted in a loss of viability upon mutation to alanine (Fig. S5B) [26], highlighting the conservation of this motif across different picornaviruses.

The viral 3C protease ($3C^{pro}$) cleaves the picornavirus capsid at two conserved glutamine-glycine (QG) pairs to liberate the viral capsid proteins VP0, VP3, and VP1 (Fig. 5A). Previous work has defined the sequence specificity of several picornavirus $3C^{pro}$ enzymes by examining both natural sequence variation and in vitro cleavage assays using synthetic peptides [27]. However, unlike other $3C^{pro}$ mediated cleavage events in the viral polyprotein, the capsid is only efficiently cleaved by the precursor protein $3CD^{pro}$ [28]. To gain insights into the sequence specificity of $3CD^{pro}$, we examined the amino acid preferences for a 10 amino acid region surrounding the protease cleavage site (P5-P5'). As expected based on the known specificity of the 3C protease [27], a strong preference for the presence of QG was observed at both $3CD^{pro}$ cleavage sites in our

188 dataset (positions P1 and P1' in the cleavage site; Fig. 5B,C). Interestingly, significant correlation in amino
189 acid preferences between the two cleavage sites was observed only at P1-P1' (Pearson's $\rho > 0.99$, $p < 10^{-16}$) and P4 (Pearson's $\rho > 0.49$, $p < 0.05$), as was the case in the enterovirus B alignments (Pearson's $\rho >$
191 0.84 and $p < 10^{-6}$ for positions P4, P1, and P'1; data not shown). Hence, the low agreement in amino acid
192 preferences observed for most positions across the two $3CD^{pro}$ cleavage sites suggests cleavage is strongly
193 dictated by positions P4, P1, and P1'.

194

195 **Identification of $3CD^{pro}$ cellular targets based on the sequence preferences of capsid encoded protease**
196 **cleavage sites**

197 In addition to cleaving the viral polyprotein, the picornavirus proteases cleave cellular factors to facilitate
198 viral replication, including both antiviral factors and cellular factors that favor viral IRES-driven translation
199 mechanism over cellular cap-dependent translation (e.g. DDX58, eIF4G, and PABP) [27,29]. As the canonical
200 $3C/3CD^{pro}$ QG cleavage site occurs on average 1.6 times per protein in the human proteome (~33,000
201 times), we sought to examine if the rich dataset we obtained for the amino acid preferences of the capsid
202 $3CD^{pro}$ cleavage sites can be used to identify novel cellular factors that are targeted by the viral protease.
203 Specifically, a position-specific score matrix (PSSM) was generated for the 10 amino acid region spanning
204 the two protease cleavage sites in the CVB3 capsid (P5-P5') based on the amino acid preferences identified
205 in our study (Fig. 5D). This PSSM was then used to query the human proteome for potential cleavage sites,
206 yielding a total of 746 cytoplasmic proteins (Fig. 5D; Supplementary Table S8). Eleven cellular factors that
207 are known to be cleaved during enterovirus infection were identified using this approach, including the
208 viral sensor Probable ATP-dependent RNA helicase DDX58 (RIG1), the immune transcription factors p65
209 (RELA) and interferon regulatory factor 7 (IRF7), and polyadenylate-binding protein 1 (PABPC1), an
210 important factor in translation initiation and mRNA stability (Supplementary Table S8) [27,30].

To evaluate whether our approach can identify novel cellular targets for the viral protease, we examined the ability of $3CD^{pro}$ to cleave eight different proteins found in the data set, focusing on those with cellular functions of potential relevance to CVB3 biology and which could be readily detected in our cell culture assay (e.g. availability of antibodies or tagged-variants, cleavage fragments of observable size, and high expression level). These included four interferon-inducible proteins (Pleckstrin Homology Domain Containing A4, PLEKHA4; Phospholipid Scramblase 1, PLSCR1; NOD-like receptor family CARD domain containing 5, NLRC5; Zinc Finger CCCH-Type Containing, Antiviral 1, ZC3HAV1) and four proteins involved in various cellular functions, namely apoptosis (MAGE Family Member D1, MAGED1), RNA processing (WD repeat domain 33, WDR33), and vesicle transport (Cyclin G Associated Kinase, GAK; Tumor Susceptibility 101, TSG101). Of these, three proteins were cleaved upon expression of the viral protease to generate fragments of the expected size (PLSCR1, PLEKHA4, and WDR33; Fig. 5E and Supplementary Table S8). Of note, while WDR33 was predicted to harbor two potential cleavage sites, only a single cleavage event was observed. Treatment with a specific $3CD^{pro}$ inhibitor, rupintrivir [31], blocked the cleavage of these proteins, indicating the effect was due to the viral protease (Fig. 5D). In contrast, five of the proteins were found to not be cleaved upon $3CD^{pro}$ expression, suggesting additional determinants are involved in the cleavage of host factors (Fig. S6). Hence, our approach correctly identified 30% of the predicted cleavage sites (3 of the 9 different cleavage sites), indicating a strong enrichment of cellular targets of the $3CD^{pro}$ in the dataset.

CONCLUSIONS

The picornavirus capsid is a highly complex structure that plays key roles in viral biology and pathogenesis. In the current study, we employ a comprehensive approach to define the effects of single amino acid mutations in the CVB3 capsid, measuring the effects of >90% of all possible mutations. We find that most mutations in the capsid are deleterious, with very few mutations showing higher fitness than the WT sequence (1.2% of all mutations). Similar results have been reported in other non-enveloped capsid proteins [32–34] as well as non-capsid viral proteins [17,35–41]. In light of these results, it is likely that the large population sizes of RNA viruses help maintain viral fitness in the face of high mutation rates and strong mutational fitness costs.

Investigation of the factors that influence MFE in the capsid revealed a strong correlation with various structural and functional attributes. These included computationally predicted effects on stability and aggregation propensity, secondary structure, and surface exposure (Fig. 2). Surprisingly, we find that MFE can be predicted with relatively high accuracy using only five parameters: natural sequence variation, the identity of the original and mutant amino acid, the predicted effect on protein stability, and relative solvent accessibility (Fig. 3). A recent study examined the ability of 46 different variant effect prediction tools to predict MFE from 31 different DMS datasets of both viral and non-viral proteins [42]. Overall, viral proteins showed the lowest predictability (Spearman's correlation of <0.5). In contrast, we were able to predict MFE using a random forest model using these above-mentioned five parameters with an accuracy similar to the best prediction obtained in this analysis for any viral or non-viral protein (Pearson's r= 0.73; Spearman's ρ = 0.73; Fig. 3B). Interestingly, SNAP2 [43], a neural network-based classifier of mutational effects that was shown to correlate well with MFE in other studies [42,44,45], correlated poorly with our data (R^2 = -0.26). Overall, considering the relative conservation of capsid structure in picornaviruses as well as

the availability of both capsid sequences and high-resolution structures for numerous members of this family, it is likely that these findings can be extrapolated to additional picornaviruses.

Incorporating site-specific amino acid preferences obtained from our DMS results into phylogenetic models was found to significantly improve model accuracy. This has been observed in DMS studies with other RNA viruses [24,39,46], and indicate that our laboratory-measured MFE capture additional information that cannot be obtained from sequence analysis alone. In addition, this approach allowed us to assess which sites show differential selection patterns as a result of the distinct environments encountered in nature and the laboratory. As expected, pressure from the adaptive immune system was found to be the major difference between these environments, with residues in antibody neutralization sites showing higher differential selection compared to other sites in the capsid (Fig. 4A). Moreover, the sites showing the highest degree of differential selection were found in known antibody neutralization sites (Fig. 4B-D). However, why these particular residues within antibody neutralization sites show differential selection, while others do not, remain to be elucidated. It has been shown that one, or a few, sites within antibody binding regions can have strong effects on escape from antibody neutralization [47], potentially explaining these findings. Interestingly, while the top three sites showing differential selection were in antibody neutralization sites, the mutation showing the fourth-highest differential selection was found in the HI loop of VP1. While not classically considered an antibody epitope, this loop has been shown to interact with an antibody fragment in the picornavirus coxsackievirus A6 [48], is known to mediate receptor binding in different picornaviruses [49,50], and to interact with host cyclophilin A to facilitate uncoating [15]. Whether these factors or others are responsible for the observed differential selection remains to be elucidated.

The CVB3 capsid encodes the information for directing myristoylation, protease cleavage, and interaction with host factors. We took advantage of our data to examine the sequence specificity and mutational tolerance of several known capsid encoded motifs. First, we examined the amino acid preferences of the CVB3 capsid myristoylation motif. We observe a strong correlation with the canonical myristoylation pattern (Prosite pattern PDOC00008), although with greater intolerance to mutations in three of the six residues in the capsid (Fig. S5). This is likely to stem from additional constraints imposed by capsid structure. On the other hand, we examined the amino acid preference of a conserved motif in VP1 that is required for $3CD^{pro}$-mediated cleavage of picornavirus capsids [26]. Our data showed a higher cost to mutation in this motif relative to other capsid positions (Fig. S5), highlighting its importance for capsid function. Finally, we examined the sequence preferences surrounding the two $3CD^{pro}$ cleavage sites. We find a strong dependence on the cleavage site residues (positions P1 and P1'; Fig. 5) and to a lesser degree position P4, with large variation in the sequence preferences across the remaining positions between the two cleavage sites. Overall, our experimentally measured MFE are congruent with existing information regarding the sequence preferences of the examined capsid motifs, yet provide in-depth insights into sequence specificity that cannot be obtained from examining natural sequence variation.

Finally, we used the amino acid preferences observed in $3CD^{pro}$ cleavage sites within the capsid to query the human genome for potential cellular targets of this protease (Fig. 5D). Using this approach, we identify 746 cytoplasmic proteins that harbor a potential $3CD^{pro}$ target sequence, including 11 proteins previously shown to be cleaved by different picornavirus 3C proteases. We then validated our approach using eight proteins, comprising nine predicted cleavage sites. Six of the predicted cleavage sites were not affected by $3CD^{pro}$ expression (Fig. S6). On the other hand, three proteins were observed to be specifically cleaved by the viral protease (Fig. 5E): WD Repeat Domain 33 (WDR33), an important factor for polyadenylation of cellular pre-mRNAs [51] that has been shown to act as a restriction factor during influenza infection [52];

299 the interferon-induced protein Phospholipid scramblase 1 (PLSCR1), which is involved in the replication
300 of numerous viruses, likely due to its ability to enhance the expression of certain interferon-stimulated
301 genes [53]; and the interferon-induced Pleckstrin Homology Domain Containing A4 (PLEKHA4), a plasma
302 membrane-localized signaling modulator [54] that is currently not known to play a role in viral infection.
303 Overall, our approach correctly predicts 30% of the identified cleavage sites. It is likely that incorporating
304 additional selection criteria, such as accessibility of the cleavage peptide in the folded structure, can be
305 used to further reduce false positives. Nevertheless, extrapolating our validation results to the larger
306 dataset suggests >200 new host targets of the protease are identified, many of which could play key roles
307 in viral biology and pathogenesis.

308

309 **FUNDING**

310 This work was funded by a grant from the Spanish Ministerio de Ciencia, Innovación y Universidades to
311 RG (BFU2017-86094-R). RG holds the Ramón y Cajal fellowship from the Spanish Ministry of Economy and
312 Competitiveness (RYC-2015-17517) and FM an FPI grant from the Spanish Ministerio de Ciencia,
313 Innovación y Universidades (BES-2016-076677).

314

315 **ACKNOWLEDGMENTS**

316 The authors would like to thank Dr. Javier O. Cifuentes for help with the interpretation of antibody
317 neutralization sites and Drs. Santiago Elena and Tzachi Hagai for critical reading of the manuscript. In
318 addition, the authors would like to acknowledge the use of the Principe Felipe Research Center (CIPF)
319 server which was co-financed by the European Union through the Operativa Program of the European
320 Regional Development Fund (ERDF/FEDER) of the Comunitat Valenciana 2014-2020.

AUTHOR CONTRIBUTIONS

FM, VL, and RG designed and performed the experiments. FM, VL, OT, AS and RG analyzed the data. FM, VL, AS, and RG wrote the manuscript. RG acquired funding.

METHODS

Viruses, cells, and plaque assays: HeLa-H1 (CRL-1958) and HEK293 (CRL-1573) cells were obtained from ATCC. All work with CVB3 was based on the Nancy infectious clone (kind gift of Dr. Marco Vignuzzi, Institute Pasteur). Cells were cultured in culture media (DMEM with 10% heat-inactivated FBS, Pen-Strep, and L-Glutamine) with FBS concentrations of 2% during infection. For plaque assays, serial dilutions of the virus were used to infect confluent HeLa-H1 cells in 6 well plates for 45 minutes, followed by overlaying the cells with a 1:1 mixture of 56°C 1.6% Agar (Arcos Organics 443570010) and 37°C 2x DMEM with 4% FBS. Two days later, plates were fixed with formaldehyde (2% final concentration) after which the agar was removed and the cells stained with crystal violet to visualize plaques.

Deep mutational scanning (DMS): The infectious clone was modified by site-directed mutagenesis to remove an XhoI site present in the capsid region (P1) and introduce an XhoI site at position 692 as well as a Kpn2I site at position 3314, generating a pCVB3-XhoI-P1-Kpn2I clone [55]. In addition, a pCVB3-XhoI-ΔP1-Kpn2I plasmid was generated by replacing the region between the XhoI and Kpn2I sites in pCVB3-XhoI-P1-Kpn2I with a short linker. To generate the template for DMS, the capsid region was amplified by PCR from pCVB3-XhoI-P1-Kpn2I with Phusion polymerase (Thermo Scientific) and primers HiFi-F (CTTTGTTGGGTTTATACCACTTAGCTCGAGAGAGG) and HiFi-R (CCTGTAGTTCCCCACATACACTGCTCCG) and gel purified (Zymoclean Gel DNA Recovery Kit). Primers spanning the full coding region of the capsid region were designed using the CodonTilingPrimers software from the Bloom lab (https://github.com/jbloomlab/CodonTilingPrimers) with the default parameters and synthesized by IDT

(Supplementary Table S1). These primers were used to perform the mutagenesis PCR on the capsid template together with the HiFi-F or HiFi-R primers in triplicate following published protocols [56] with the exception that 10 rounds of mutagenesis were performed for libraries 1 and 2, while a second round of 7 mutagenesis cycles was performed for library 3 to increase the number of mutation per clone. The products were gel purified and ligated to an XhoI and Kpn2I digested and gel purified pCVB3-XhoI-ΔP1-Kpn2I using NEBuilder® HiFi DNA Assembly reaction (NEB) for 25 minutes. Mutagenesis efficiency was evaluated by the transformation of the assembled plasmids into NZY5α competent cells (NZY Tech), Sanger sequencing of 18-23 clones per library, and mutation analysis using the Sanger Mutant Library Analysis script (https://github.com/jbloomlab/SangerMutantLibraryAnalysis). Subsequently, the assembled plasmid reactions were purified using a Zymo DNA Clean & Concentrator-5 kit (Zymo Research) and used to electroporate MegaX DH10B T1R Electrocomp cells (ThermoFisher) using a Gene Pulser XCell electroporator (BioRad) according to the manufacturer's protocol. Cells were then grown overnight in a 50 mL liquid culture at 33°C and DNA purified using the PureLink HiPure plasmid midiprep kit (Invitrogen). Transformation efficiency was estimated by plating serial dilutions of the transformation on agar plates. In total, 4.44×10^5, 1.46×10^5, and 2.19×10^5 transformants were obtained for lines 1, 2, and 3, respectively. Viral genomic RNA was then transcribed from SalI linearized, gel-purified full-length plasmids using the TranscriptAid T7 kit (ThermoScientific), and four electroporations were performed using 4×10^6 HeLa-H1 cells in a 4mm cuvette in 400μL of calcium and magnesium-free PBS using with 8μg of RNA in a Gene Pulser XCell (BioRad) set to 240V and 950uF. Electroporated cells were then pooled, and one fourth was cultured for 9 hours to produce the passage 0 virus (P0). Following three freeze-thaw cycles, 2×10^6 plaque-forming units (PFU) were used to infect a 90% confluent 15cm plate in 2.5mL of infection media for 1 hour. Cells were then washed with PBS and incubated in 12 mL of infection media for 9 hours. Finally, cells were subjected to 3 freeze-thaw cycles, debris removed by centrifugation at 500xg and the supernatants

collected to generate P1 virus stocks. All infection produced > $2.38x10^6$ PFU in P0 and > $1.2x10^7$ PFU in P1 as judged by plaque assay.

NGS analysis:

Libraries were prepared following published protocols [57] and each library was run on a Novaseq6000 2x150 at a maximum of 30G per lane to reduce potential index hopping. Reads trimming was performed using fastp [58] (command: -max_len1 150 --max_len2 150 --length_required 150 -x -Q -A), unsorted bam files were generated from fastq files using Picard tools FastqToSam (version 2.2.4) and merged into a single bam using the cat command of Samtools (version 1.5). The duplex pipeline was then implemented (https://github.com/KennedyLabUW/Duplex-Sequencing/UnifiedConsensusMaker.py) using the UnifiedConsensusMaker.py script and a minimum family size of 3, a cutoff of 0.9 for consensus calling, and an N cutoff of 0.3. The single-stranded consensus files (SSCS) were then aligned using BWA mem (version 0.7.16), sorted using Samtools, size selected to be 133 bp long using VariantBam [59], unaligned reads were discarded (Samtools view command with -F 4), and the resulting bam file indexed with Samtools. Subsequently, fgbio (http://fulcrumgenomics.github.io/fgbio/; version 1.1.0) was used to hard-clip 10 bp from each end and upgrade all clipping to hard-clip (-c Hard --upgrade-clipping true --read-one-five-prime 10 --read-one-three-prime 10 --read-two-five-prime 10 --read-two-three-prime 10). Variant bam was then used to keep all reads that were between 50-150bp, well-mapped, and had either no indels and less than 5 mutations (command –r {"":{"rules":[{"ins":[0,0],"del":[0,0],"nm":[0,4], "mate_mapped":true,"fr":true,"length":[50,150]}]}}'). Finally, the codons in each read were identified using the VirVarSeq [60] Codon_table.pl script using a minimum read quality of 20. A custom R script was then used to generate a codon counts table for each codon position by eliminating all codons containing ambiguous nucleotides and codons with a strong strand bias (StrandOddsRatio > 4), as well as all codons that are reached via a single mutation (available at https://github.com/RGellerLab/CVB3_Capsid_DMS).

Amino acid preferences and mutational fitness effects were determined using DMStools2 [19] with the Bayesian option and the default settings.

Structural analyses: The crystal structure PDB:4GB3 [61] was used for all structural analysis. The effects of mutations on aggregation were determined using TANGO version 2.3.1 [22] using the default settings and the effect on stability on the monomer and pentamer was determined using FoldX 4 [21] using the default settings. For the latter, the pentamer subunits were renamed to unique letters, all mutations between the reference sequence and the structure sequence were introduced using the BuildModel command, the structure was optimized using the RepairPDB command 5 or 10 times for the pentamer or monomer, respectively, and then the effects of the mutations were predicted using the BuildModel command (modified PDB files can be found at https://github.com/RGellerLab/CVB3_Capsid_DMS). Secondary structure and RSA were obtained from DSSP (http://swift.cmbi.ru.nl/gv/dssp/) using the dms_tools2.dssp function of dms_tools2, while interface, surface, and core residues as well as residue contact number, and presence in the two, three, and five-fold axes were obtained from ViprDB (http://viperdb.scripps.edu/) [62]. Distance from the center was calculated with Pymol using the Distancetoatom.py script on the monomer or pentamer.

Generation and evaluation of CVB3 capsid mutants: The PCR of the capsid region used as a template for DMS was phosphorylated and cloned into a SmaI digested pUC19 vector for use in the mutagenesis reactions (pUC19-HiFi-P1). For each mutant, non-overlapping primers containing the mutation in the middle of the forward primer were used to introduce the mutation with Phusion polymerase, followed by DpnI (Thermo Scientific) treatment, phosphorylation, ligation, and transformation of chemically competent bacteria. Successful mutagenesis was verified by Sanger sequencing. Subsequently, the capsid region was subcloned into pCVB3-XhoI-ΔP1-Kpn2I using XhoI and Kpn2I sites. Plasmids were then linearized with MluI and 2μg of plasmid was transfected into $5x10^5$ HEK293 cells together with a plasmid encoding the T7 polymerase [63] (Addgene 65974) using calcium phosphate. Briefly, an equal volume of 2x

HBS (274mM NaCl, 10mM KCl, 1.4mM Na_2HPO_4) was added dropwise to DNA containing 0.25M $CaCl_2$ while mixing, incubated 15 minutes at RT, and then added dropwise to cells. Following 48 hours, passage 0 (P0) virus was collected and titered by plaque assay. From this, 10^5 PFU were used to infect 90% confluent 6 well HeLa-H1 cells (MOI 0.1) for 1 hour at 37°C, after which the cells were washed twice with PBS and 2mL of infection media added. Cells were then incubated until CPE was observed. Emerging viral populations were titered by plaque assay and the capsid region sequenced to ensure no compensatory mutations or reversions arose during replication. The fitness of these mutants was then tested by direct competition with a marked reference virus using a Taqman RT-PCR method [20]. Briefly, in quadruplicates, confluent HeLa-H1 cells in a 24 well plate were infected with 200µL of a 1:1 mixture of $4x10^3$ PFU (MOI 0.01) of the test and marked reference viruses for 45 minutes. Subsequently, the inoculum was removed, the cells were washed twice with PBS, 200 µL of infection media was added, and the cells were incubated for 24 hours at 37°C. Finally, cells were subjected to 3 freeze-thaw cycles, debris removed by centrifugation at 500xg, the supernatants collected and treated with 2uL of RNase-Free DNaseI (ThermoFisher) for 15 minutes at 37°C, and viral RNA extracted using the *Quick*-RNA™ Viral Kit (Zymo Research), eluting in 20µl. Quantification of the replication of each mutant versus the reference was performed using Luna® Universal Probe One-Step RT-qPCR kit (New England BioLabs) containing 3uL of total RNA, 0.4µM of each qPCR primers and 0.2µM of each probe. The standard curve was performed using 10-fold dilutions of RNA extracted from 10^7 PFU of wild-type and reference viruses. All samples were performed with three technical replicates. The relative fitness (W) of each mutant versus the common marked reference virus was calculated using the formula $W = [R(t)/R(0)]^{1/t}$, where R(0) and R(t) represents the ratio of the mutant to the reference virus genomes in the initial mixture used for the infection and after 1 day (t=1), respectively [20,64].

Sequence variability and phylogenetic analyses: Amino acid variability was assessed using Shannon entropy. Briefly, all available, non-identical, full-genome CVB3, CVB, or Enterovirus B sequences were

438 downloaded from Virus Pathogen Resource [65] (www.viprbrc.org) and codon-aligned using the DECIPHER
439 package in R (available at https://github.com/RGellerLab/CVB3_Capsid_DMS). All alignment positions not
440 present in our reference strain were removed, and a custom R script was used to calculate Shannon
441 entropy. For phylogenetic and differential selection analyses, PhyDMS was run using the default settings
442 on an alignment of CVB3 genomes that was processed with the phydms_prealignment module and using
443 the average preferences from the three DMS replicates.

444 **Identification of 3CD^{pro} cleavage sites in the human proteome:** The amino acid preferences (the relative
445 enrichment of each amino acid at each position standardized to 1) was used to generate in silico 1000
446 peptides spanning the 10 amino acid region surrounding each cleavage site using a custom R script
447 (available at https://github.com/RGellerLab/CVB3_Capsid_DMS). Specifically, for each peptide position,
448 100 peptides were generated that encoded each amino acid at a frequency corresponding to its
449 preference observed in the DMS results, with the remaining positions unchanged. The resulting 1000
450 peptides from each cleavage site were uploaded to PSSMSearch [66] (http://slim.icr.ac.uk/pssmsearch/)
451 using the default setting (psi_blast IC). Results were filtered to remove proteins indicated to be secreted,
452 lumenal, or extracellular in the Warnings column. To test whether proteins were cleaved by the viral 3CD
453 protease, the corresponding region was PCR amplified from the Nancy infectious clone (primers 3C-For:
454 TATTCTCGAGACCATGGGCCCTGCCTTTGAGTTCG and 3D-Rev:
455 TATTGCGGCCGCCTAGAAGGAGTCCAACCATTTCCT) and cloned into the pIRES plasmid (Clonetech) using
456 the restriction sites XhoI and NotI (pIRES-3CD^{pro}). For analysis of fusion proteins, HEK293 cells were
457 transfected with GFP-PLEKHA4 (kind gift of Dr. Jeremy Baskin, Cornell University), GFP-PLSCR1 (kind gift
458 of Dr. Serge Benichou, Institut Cochin), FLAG-NLCR5 (Addgene #37521), HA-ZC3HAV1 (Addgene #45907),
459 or the control plasmid FLuc-eGFP (Addgene #90170) together with the pIRES-3CD^{pro} plasmid using
460 Lipofectamine 2000. Following 24 hours, proteins were collected by lysing in lysis buffer (50mM TRIS-HCl,
461 150mM NaCl, 1% NP40 and protease inhibitor cocktail [Complete Mini EDTA-free, Roche]) and subjected

462 to western blotting with the corresponding antibody (anti-GFP, Santa Cruz sc-9996; Anti FLAG, Santa Cruz
463 sc-166335; anti-HA, Santa Cruz, sc-7392). For analysis of endogenous proteins, $3CD^{pro}$ was expressed for
464 48 hours before cell lysis, and western blotting using antibodies against WDR33 (Santa Cruz sc-374466),
465 TSG101 (Santa Cruz sc-136111), GAK (Santa Cruz sc-137053), and MAGED1 (Santa Cruz sc-393291). When
466 indicated, the $3C^{pro}$ inhibitor rupintrivir (Tocris Biosciences) was added at a concentration of 2 μM for the
467 last 24 hours before collection. The predicted molecular weight of cleaved fragments was calculated using
468 the mw function of the Peptides R package (version 2.4.2).

469 **Statistical analyses:** All statistical analyses were performed in R and were two-tailed. For random forest
470 prediction, the R RandomForest package (version 4.6-14) was employed using the default setting with an
471 mtry of 10, and for the linear model, the formula lm(MFE ~ enterovirus B entropy + WT amino acid *
472 mutant amino acid + predicted effect of mutations on stability in the pentamer + relative surface
473 exposure) was used (available at https://github.com/RGellerLab/CVB3_Capsid_DMS). Sequence logoplots
474 were producing using Logolas [67].

475 **Data availability:** Unaligned bam files have been uploaded to SRA (Accession SAMN15437545-
476 SAMN15437555; SRA 15437545-15437555). The scripts and data required to obtain the codon count
477 tables for all samples, to perform the random forest and linear model predictions, to generate the
478 peptides for use with PSSMsearch, as well as the sequence alignments and modified structure files for
479 FoldX analysis can be found on Github (https://github.com/RGellerLab/CVB3_Capsid_DMS).

REFERENCES

1. Harrison, S. C. Principles of Virus Structure. in *Fields Virology* (eds. Knipe, D. M. & Howley, P. M.) 52–86 (Wolters Kluwer Health/Lippincott Williams & Wilkins, 2013).

2. Hunter, E. Virus Assembly. in *Fields Virology* (eds. Knipe, D. M. & Howley, P. M.) 127–152 (Wolters Kluwer Health/Lippincott Williams & Wilkins, 2013).

3. Perlmutter, J. D. & Hagan, M. F. Mechanisms of virus assembly. *Annu. Rev. Phys. Chem.* **66**, 217–39 (2015).

4. Geller, R., Vignuzzi, M., Andino, R. & Frydman, J. Evolutionary constraints on chaperone-mediated folding provide an antiviral approach refractory to development of drug resistance. *Genes Dev.* **21**, 195–205 (2007).

5. Macejak, D. G. & Sarnow, P. Association of heat shock protein 70 with enterovirus capsid precursor P1 in infected human cells. *J. Virol.* **66**, 1520–1527 (1992).

6. Callaway, A., Giesman-Cookmeyer, D., Gillock, E. T., Sit, T. L. & Lommel, S. A. The multifunctional capsid proteins of plant RNA viruses. *Annual Review of Phytopathology* (2001). doi:10.1146/annurev.phyto.39.1.419

7. Jiang, P. *et al.* Picornavirus Morphogenesis. *Microbiol. Mol. Biol. Rev.* **78**, 418–437 (2014).

8. Fields, B. N., Knipe, D. M. & Howley, P. M. *Fields virology*. (Wolters Kluwer Health/Lippincott Williams & Wilkins, 2013).

9. Rossmann, M. G., He, Y. & Kuhn, R. J. Picornavirus-receptor interactions. *Trends in Microbiology* (2002). doi:10.1016/S0966-842X(02)02383-1

10. Helenius, A. Virus Entry and Uncoating. in *Fields Virology* (eds. Knipe, D. M. & Howley, P. M.) 87–104 (Wolters Kluwer Health/Lippincott Williams & Wilkins, 2013).

11. Cifuente, J. O. & Moratorio, G. Evolutionary and Structural Overview of Human Picornavirus Capsid Antibody Evasion. *Front. Cell. Infect. Microbiol.* **9**, 1–11 (2019).

12. Heise, M. T. & Virgin, H. W. Pathogenesis of viral infection. in *Fields Virology* (eds. Knipe, D. M. & Howley, P. M.) **1**, 254–285 (Wolters Kluwer Health/Lippincott Williams & Wilkins, 2013).

13. Racaniello, V. R. Picornaviridae: The Viruses and Their Replication. in *Fields Virology* (eds. Knipe,

M. D. & Howley, M. P.) 453–489 (Philadelphia : Wolters Kluwer Health/Lippincott Williams & Wilkins, c2013., 2013).

14. Thibaut, H. J. *et al.* Binding of Glutathione to Enterovirus Capsids Is Essential for Virion Morphogenesis. *PLoS Pathog.* **10**, e1004039 (2014).

15. Qing, J. *et al.* Cyclophilin A Associates with Enterovirus-71 Virus Capsid and Plays an Essential Role in Viral Infection as an Uncoating Regulator. *PLoS Pathog.* (2014). doi:10.1371/journal.ppat.1004422

16. Corbic Ramljak, I. *et al. Cellular N-myristoyltransferases play a crucial picornavirus genus-specific role in viral assembly, virion maturation, and infectivity*. *PLOS Pathogens* **14**, (2018).

17. Bloom, J. D. An experimentally determined evolutionary model dramatically improves phylogenetic fit. *Mol. Biol. Evol.* **31**, 1956–78 (2014).

18. Schmitt, M. W. *et al.* Detection of ultra-rare mutations by next-generation sequencing. *Proc. Natl. Acad. Sci.* **109**, 14508–14513 (2012).

19. Bloom, J. D. Software for the analysis and visualization of deep mutational scanning data. *BMC Bioinformatics* **16**, 168 (2015).

20. Moratorio, G. *et al.* Attenuation of RNA viruses by redirecting their evolution in sequence space. *Nat. Microbiol.* **2**, 17088 (2017).

21. Schymkowitz, J. *et al.* The FoldX web server: an online force field. *Nucleic Acids Res.* **33**, W382-8 (2005).

22. Fernandez-Escamilla, A.-M., Rousseau, F., Schymkowitz, J. & Serrano, L. Prediction of sequence-dependent and mutational effects on the aggregation of peptides and proteins. *Nat. Biotechnol.* **22**, 1302–1306 (2004).

23. Hilton, S. K., Doud, M. B. & Bloom, J. D. Phydms: Software for phylogenetic analyses informed by deep mutational scanning. *PeerJ* (2017). doi:10.7717/peerj.3657

24. Bloom, J. D. Identification of positive selection in genes is greatly improved by using experimentally informed site-specific models. *Biol. Direct* **12**, 1 (2017).

25. Bologna, G., Yvon, C., Duvaud, S. & Veuthey, A. L. N-terminal myristoylation predictions by

534 ensembles of neural networks. *Proteomics* **4**, 1626–1632 (2004).

535 26. Kristensen, T. & Belsham, G. J. Identification of a short, highly conserved, motif required for
536 picornavirus capsid precursor processing at distal sites. *PLoS Pathog.* **15**, e1007509 (2019).

537 27. Laitinen, O. H. *et al.* Enteroviral proteases: structure, host interactions and pathogenicity. *Rev.*
538 *Med. Virol.* **26**, 251–267 (2016).

539 28. Ypma-Wong, M. F., Dewalt, P. G., Johnson, V. H., Lamb, J. G. & Semler, B. L. Protein 3CD is the
540 major poliovirus proteinase responsible for cleavage of the p1 capsid precursor. *Virology* **166**,
541 265–270 (1988).

542 29. Sun, D., Chen, S., Cheng, A. & Wang, M. Roles of the picornaviral 3c proteinase in the viral life
543 cycle and host cells. *Viruses* **8**, 1–22 (2016).

544 30. Jagdeo, J. M. *et al.* N-Terminomics TAILS Identifies Host Cell Substrates of Poliovirus and
545 Coxsackievirus B3 3C Proteinases That Modulate Virus Infection. *J. Virol.* **92**, 1–23 (2018).

546 31. Dragovich, P. S. *et al.* Structure-Based Design, Synthesis, and Biological Evaluation of Irreversible
547 Human Rhinovirus 3C Protease Inhibitors. 4. Incorporation of P 1 Lactam Moieties as l -Glutamine
548 Replacements. *J. Med. Chem.* **42**, 1213–1224 (1999).

549 32. Hartman, E. C. *et al.* Quantitative characterization of all single amino acid variants of a viral
550 capsid-based drug delivery vehicle. *Nat. Commun.* **9**, 1385 (2018).

551 33. Ogden, P. J., Kelsic, E. D., Sinai, S. & Church, G. M. Comprehensive AAV capsid fitness landscape
552 reveals a viral gene and enables machine-guided design. *Science* **366**, 1139–1143 (2019).

553 34. Acevedo, A., Brodsky, L. & Andino, R. Mutational and fitness landscapes of an RNA virus revealed
554 through population sequencing. *Nature* **505**, 686–90 (2014).

555 35. Du, Y. *et al.* Annotating Protein Functional Residues by Coupling High-Throughput Fitness Profile
556 and Homologous-Structure Analysis. *MBio* **7**, 1–13 (2016).

557 36. Wu, N. C. *et al.* Functional Constraint Profiling of a Viral Protein Reveals Discordance of
558 Evolutionary Conservation and Functionality. *PLoS Genet.* **11**, e1005310 (2015).

559 37. Thyagarajan, B. & Bloom, J. D. The inherent mutational tolerance and antigenic evolvability of
560 influenza hemagglutinin. *Elife* **3**, 1–26 (2014).

561 38. Haddox, H. K. *et al.* Experimental Estimation of the Effects of All Amino-Acid Mutations to HIV's
562 Envelope Protein on Viral Replication in Cell Culture. *PLOS Pathog.* **12**, e1006114 (2016).

563 39. Doud, M. B. & Bloom, J. D. Accurate Measurement of the Effects of All Amino-Acid Mutations on
564 Influenza Hemagglutinin. *Viruses* **8**, 1–17 (2016).

565 40. Ashenberg, O., Padmakumar, J., Doud, M. B. & Bloom, J. D. Deep mutational scanning identifies
566 sites in influenza nucleoprotein that affect viral inhibition by MxA. *PLoS Pathog.* **13**, e1006288
567 (2017).

568 41. Hom, N., Gentles, L., Bloom, J. D. & Lee, K. K. Deep Mutational Scan of the Highly Conserved
569 Influenza A Virus M1 Matrix Protein Reveals Substantial Intrinsic Mutational Tolerance. *J. Virol.*
570 **93**, 1–16 (2019).

571 42. Livesey, B. J. & Marsh, J. A. Using deep mutational scanning to benchmark variant effect
572 predictors and identify disease mutations. *Mol. Syst. Biol.* **16**, 1–12 (2020).

573 43. Hecht, M., Bromberg, Y. & Rost, B. Better prediction of functional effects for sequence variants.
574 *BMC Genomics* **16**, S1 (2015).

575 44. Gray, V. E., Hause, R. J., Luebeck, J., Shendure, J. & Fowler, D. M. Quantitative Missense Variant
576 Effect Prediction Using Large-Scale Mutagenesis Data. *Cell Syst.* **6**, 116-124.e3 (2018).

577 45. Reeb, J., Wirth, T. & Rost, B. Variant effect predictions capture some aspects of deep mutational
578 scanning experiments. *BMC Bioinformatics* **21**, 107 (2020).

579 46. Haddox, H. K., Dingens, A. S., Hilton, S. K., Overbaugh, J. & Bloom, J. D. Mapping mutational
580 effects along the evolutionary landscape of HIV envelope. *Elife* **7**, e34420 (2018).

581 47. Lee, J. M. *et al.* Mapping person-to-person variation in viral mutations that escape polyclonal
582 serum targeting influenza hemagglutinin. *Elife* **8**, 1–28 (2019).

583 48. Xu, L. *et al.* Atomic structures of Coxsackievirus A6 and its complex with a neutralizing antibody.
584 *Nat. Commun.* (2017). doi:10.1038/s41467-017-00477-9

585 49. Belnap, D. M. *et al.* Three-dimensional structure of poliovirus receptor bound to poliovirus. *Proc.*
586 *Natl. Acad. Sci. U. S. A.* (2000). doi:10.1073/pnas.97.1.73

587 50. Xing, L. *et al.* Distinct cellular receptor interactions in poliovirus and rhinoviruses. *EMBO J.* **19**,

1207–16 (2000).

51. Chan, S. L. *et al.* CPSF30 and Wdr33 directly bind to AAUAAA in mammalian mRNA 3′ processing. *Genes Dev.* **28**, 2370–2380 (2014).

52. Brass, A. L. *et al.* The IFITM proteins mediate cellular resistance to influenza A H1N1 virus, West Nile virus, and dengue virus. *Cell* **139**, 1243–54 (2009).

53. Kodigepalli, K. M., Bowers, K., Sharp, A. & Nanjundan, M. Roles and regulation of phospholipid scramblases. *FEBS Lett.* **589**, 3–14 (2015).

54. Shami Shah, A. *et al.* PLEKHA4/kramer Attenuates Dishevelled Ubiquitination to Modulate Wnt and Planar Cell Polarity Signaling. *Cell Rep.* **27**, 2157-2170.e8 (2019).

55. Bou, J. V., Geller, R. & Sanjuán, R. Membrane-Associated Enteroviruses Undergo Intercellular Transmission as Pools of Sibling Viral Genomes. *Cell Rep.* **29**, 714-723.e4 (2019).

56. Dingens, A. S., Haddox, H. K., Overbaugh, J. & Bloom, J. D. Comprehensive Mapping of HIV-1 Escape from a Broadly Neutralizing Antibody. *Cell Host Microbe* **21**, 777-787.e4 (2017).

57. Kennedy, S. R. *et al.* Detecting ultralow-frequency mutations by Duplex Sequencing. *Nat. Protoc.* **9**, 2586–2606 (2014).

58. Chen, S., Zhou, Y., Chen, Y. & Gu, J. fastp: an ultra-fast all-in-one FASTQ preprocessor. *Bioinformatics* **34**, i884–i890 (2018).

59. Wala, J., Zhang, C.-Z., Meyerson, M. & Beroukhim, R. VariantBam: filtering and profiling of next-generational sequencing data using region-specific rules. *Bioinformatics* **32**, 2029–2031 (2016).

60. Verbist, B. M. P. *et al.* VirVarSeq: A low-frequency virus variant detection pipeline for Illumina sequencing using adaptive base-calling accuracy filtering. *Bioinformatics* **31**, 94–101 (2015).

61. Yoder, J. D., Cifuente, J. O., Pan, J., Bergelson, J. M. & Hafenstein, S. The Crystal Structure of a Coxsackievirus B3-RD Variant and a Refined 9-Angstrom Cryo-Electron Microscopy Reconstruction of the Virus Complexed with Decay-Accelerating Factor (DAF) Provide a New Footprint of DAF on the Virus Surface. *J. Virol.* **86**, 12571–12581 (2012).

62. Carrillo-Tripp, M. *et al.* VIPERdb2: an enhanced and web API enabled relational database for structural virology. *Nucleic Acids Res.* **37**, D436-42 (2009).

63. Yun, T. *et al.* Efficient reverse genetics reveals genetic determinants of budding and fusogenic differences between Nipah and Hendra viruses and enables real-time monitoring of viral spread in small animal models of henipavirus infection. *J. Virol.* **89**, 1242–53 (2015).

64. Carrasco, P., Daròs, J. A., Agudelo-Romero, P. & Elena, S. F. A real-time RT-PCR assay for quantifying the fitness of tobacco etch virus in competition experiments. *J. Virol. Methods* (2007). doi:10.1016/j.jviromet.2006.09.020

65. Pickett, B. E. *et al.* ViPR: an open bioinformatics database and analysis resource for virology research. *Nucleic Acids Res.* **40**, D593-8 (2012).

66. Krystkowiak, I., Manguy, J. & Davey, N. E. PSSMSearch: a server for modeling, visualization, proteome-wide discovery and annotation of protein motif specificity determinants. *Nucleic Acids Res.* **46**, W235–W241 (2018).

67. Dey, K. K., Xie, D. & Stephens, M. A new sequence logo plot to highlight enrichment and depletion. *BMC Bioinformatics* **19**, 473 (2018).

630 **Table 1:** Incorporation of DMS results in evolutionary models better describes natural CVB3 evolution
631 compared to standard codon models.

Model	ΔAIC	LogLikelihood	Parameters	Parameter Values
ExpCM	0.00	-14580.51	6	beta=2.18, kappa=7.47, omega=0.16
Goldman-Yang M5	4187.56	-16668.29	12	alpha_omega=0.30, beta_omega=10.00, kappa=7.15
Averaged ExpCM	4303.74	-16732.38	6	beta=0.61, kappa=7.55, omega=0.02
Goldman-Yang M0	4371.26	-16761.14	11	kappa=7.14, omega=0.02

632

633 **FIGURE LEGENDS:**

634 **Figure 1. Deep mutational scanning (DMS) of the CVB3 capsid.**

635 **A.** Overview of the deep mutational scanning experimental approach. A mutagenesis PCR was performed
636 using an external reverse primer and a pool of forward mutagenic primers targeting each capsid codon
637 that encode degenerate nucleotides (NNN) at the codon matching position. Similarly, a reverse
638 mutagenesis PCR reaction was performed. The products of these PCRs were joined using the external
639 primers and cloned into a CVB3 infectious clone to generate the mutagenized libraries. This process was
640 performed in triplicate, generating 3 libraries (Mut Library 1-3). Viral genomic RNA (vRNA) produced from
641 the mutant libraries was electroporated into cells to generate high diversity CVB3 populations (Mut Virus
642 1-3). The relative frequency of each mutation relative to the WT amino acid was then determined in both
643 the mutagenized libraries and the resulting virus populations via high-fidelity duplex sequencing. **B.** The
644 average rate of double or triple mutations per codon observed in the mutagenized libraries (Mut Library
645 1-3), the resulting mutagenized virus (Mut Virus 1-3), as well as controls for the error rate of the
646 amplification and sequencing process (PCR and RT-PCR) or the WT unmutagenized virus (WT Virus 1-2).
647 Single mutations per codon were omitted from the analysis to increase the signal-to-noise ratio. **C.** Venn
648 diagram showing the number of amino acid mutations observed in the mutagenized libraries.

649

650 **Figure 2. Mutational fitness effects across the CVB3 capsid and their correlation with structural,**
651 **evolutionary, and immunological attributes.**

652 **A.** Overview of the mutational fitness effects (MFE) across the CVB3 capsid. Bottom: a heatmap
653 representing the MFE of all mutations observed at each capsid site. Green indicates no data available
654 (ND), and the positions of the mature viral proteins (VP1-4) or antibody neutralization sites (nAb) are
655 indicated above. Top: A 21 amino acid sliding window analysis of the average sequence variation in CVB3

656 genomes (Shannon entropy; black line) or the average MFE (red line). **B.** Correlation between derived MFE
657 and variation in enterovirus B sequence alignments (Shannon entropy). **C.** Violin plot of MFE in antibody
658 neutralization sites versus other capsid sites. **D-G**. Boxplots of MFE as a function of secondary structure
659 (D), position in the capsid (E), or the predicted effect of mutations on stability (F) or aggregation
660 propensity (G). Two-sided Mann-Whitney or Kruskal-Wallis tests were used for 2 or 3 category
661 comparisons, respectively.

662

663 **Figure 3. Prediction of MFE based on structural and sequence information.**

664 **A.** The top 10 predictors identified in a random forest model for explaining MFE in the CVB3 capsid based
665 on the percent of mean squared error (MSE) increase. **B.** Hexagonal plot showing the correlation between
666 MFE predicted using a random forest algorithm trained on the top 5 variables versus observed MFE. The
667 random forest model was trained on 70% of the data, and then tested on the remaining 30% (shown).
668 RSA, relative surface area.

669

670 **Figure 4. Antibody neutralization sites show differential selection between laboratory conditions and**
671 **nature.**

672 **A.** Violin plot showing the sum of absolute differential selection observed at capsid sites comprising
673 antibody neutralization epitopes (nAb) versus all other capsid sites. **B-C.** Logoplots showing the observed
674 differential selection of sites in the EF loop or BC loop. The WT sequence is indicated in red. **D.** The CVB3
675 capsid pentamer (PDB:4GB3), colored according to the amount of differential selection. The BC and EF
676 loops are shown next to the structure together with the sidechains for sites showing the highest
677 differential selection.

Figure 5. Sequence preference of capsid 3CD^{pro} cleavage sites and their use for the identification of novel cellular targets of the viral protease.

A. Overview of the CVB3 capsid maturation pathway. The CVB3 capsid precursor P1 is co-translationally cleaved by the viral 2A protease. P1 is then myristoylated and cleaved by the viral 3CD^{pro} to generate the capsid proteins VP0, VP3, and VP1. Finally, upon assembly and genome encapsidation, VP0 is further cleaved into VP4 and VP2 in a protease independent manner to generate the mature capsid. Red and black astrickses indicated 3CD^{pro} or protease independent cleavage events, respectively. **B-C.** Logoplots showing amino acid preferences for the 10 amino acid region spanning the 3CD^{pro} cleavage sites (P1-P'1) of both VP0/VP3 and VP3/VP1 in the DMS dataset. **D.** Overview of the bioinformatic pipeline for identification of novel 3CD^{pro} cellular targets using the amino acid preferences for the capsid cleavage sites from our DMS study. A position-specific scoring matrix (PSSM) was generated based on the amino acid preferences for the 10 amino acid region spanning the two 3CD^{pro} cleavages sites. This PSSM was then used to query the human genome for potential cellular targets, and non-cytoplasmic proteins were filtered out, yielding 746 proteins. **E.** The cellular proteins PLSCR1, PLEKHA4, and WDR33 are cleaved by 3CD^{pro}. Western blot analysis of cells cotransfected with 3CD^{pro} and GFP-PLSCR1 or GFP-PLEKHA4 and probed with a GFP antibody or transfected with 3CD^{pro} and probed using a WDR33 antibody. When indicated, the 3CD^{pro} inhibitor rupintrivir was included to ensure cleavage was mediated by the viral protease. Red arrows indicate cleavage products of the expected size (GFP-PLSCR1 full length = 64 kDa, cleaved N-terminus = 36 kDa; GFP-PLEKHA4 full length = 118, cleaved N-terminus = 72 kDa; WDR33 full length = 146 kDa, cleaved N-terminus = 72 kDa) . * $p < 0.05$, *** $p < 0.001$.

Supplementary Figure S1. Sanger analysis of DMS libraries.

A. The number of mutated codons per clone. **B.** Original and mutated base for each mutation. **C.** The number of nucleotide changes per codon. **D.** Cumulative fraction of mutations versus the codon position. **E.** Location of both mutations and indels across the capsid sequence.

Supplementary Figure S2. Results of high-fidelity duplex sequencing.

A. The relative frequency of the mutated base within each mutated codon. **B.** The relative frequency of each mutation type.

Supplementary Figure S3. Correlation of amino acid preferences observed in experimental replicates.

Hexagonal bin plots showing the correlation of amino acid preferences between the three experimental replicates. Spearman's correlation coefficient and p-value are shown above each plot.

Supplementary Figure S4. Prediction of mutational fitness effects using random forest or linear models.

A. Hexagonal bin plot showing the correlation between actual and predicted MFE derived from a random forest model using all 52 variables. The model was trained on 70% of the data and tested on the remaining 30% of the data (shown). **B.** Variable importance obtained from the random forest model. **C.** Linear model using the top five parameters of the random forest model. See supplementary Table S6 for parameter description.

Supplementary Figure S5. Sequence preferences of capsid encoded motifs

A. Amino acid preferences of the CVB3 myristoylation motif. The canonical Prosite myristoylation motif is indicated above, with curly brackets indicating disfavored amino acids and square brackets indicating tolerated amino acids. **B.** WCPRP motif required for $3CD^{pro}$ cleavage of P1. Asterisks indicate analogous positions in FMDV shown to be essential for viability [26].

Supplementary Figure S6. Evaluation of select hits identified as potential $3CD^{pro}$ target proteins.

Western blots of cells transfected with $3CD^{pro}$ and probed for the indicated endogenous protein, or cotransfected with $3CD^{pro}$ and the indicated fusion protein and blotted for the tag. Each experiment was performed twice. When indicated, the $3C^{pro}$ inhibitor rupintrivir was added.

Figure 1. Mattenberger et al.

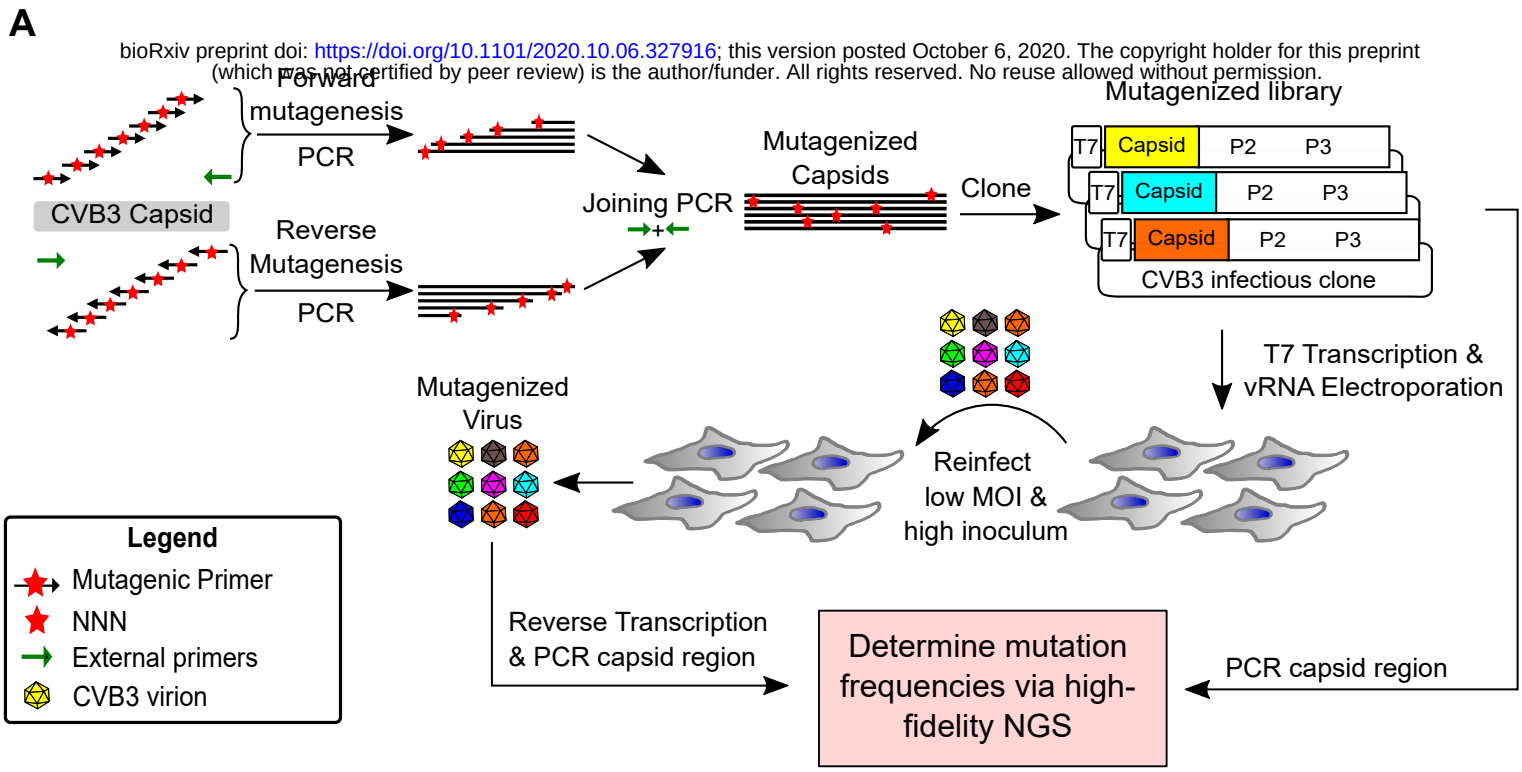

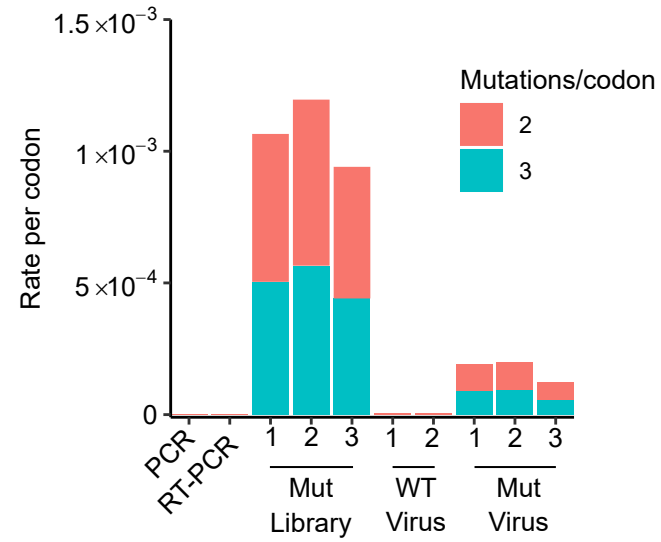

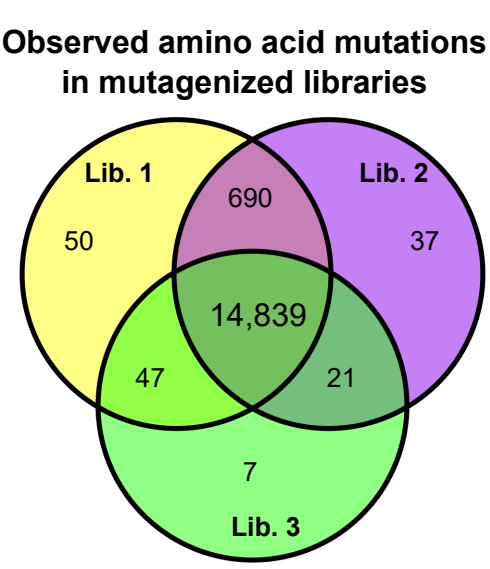

Figure 2. Mattenberger et al.

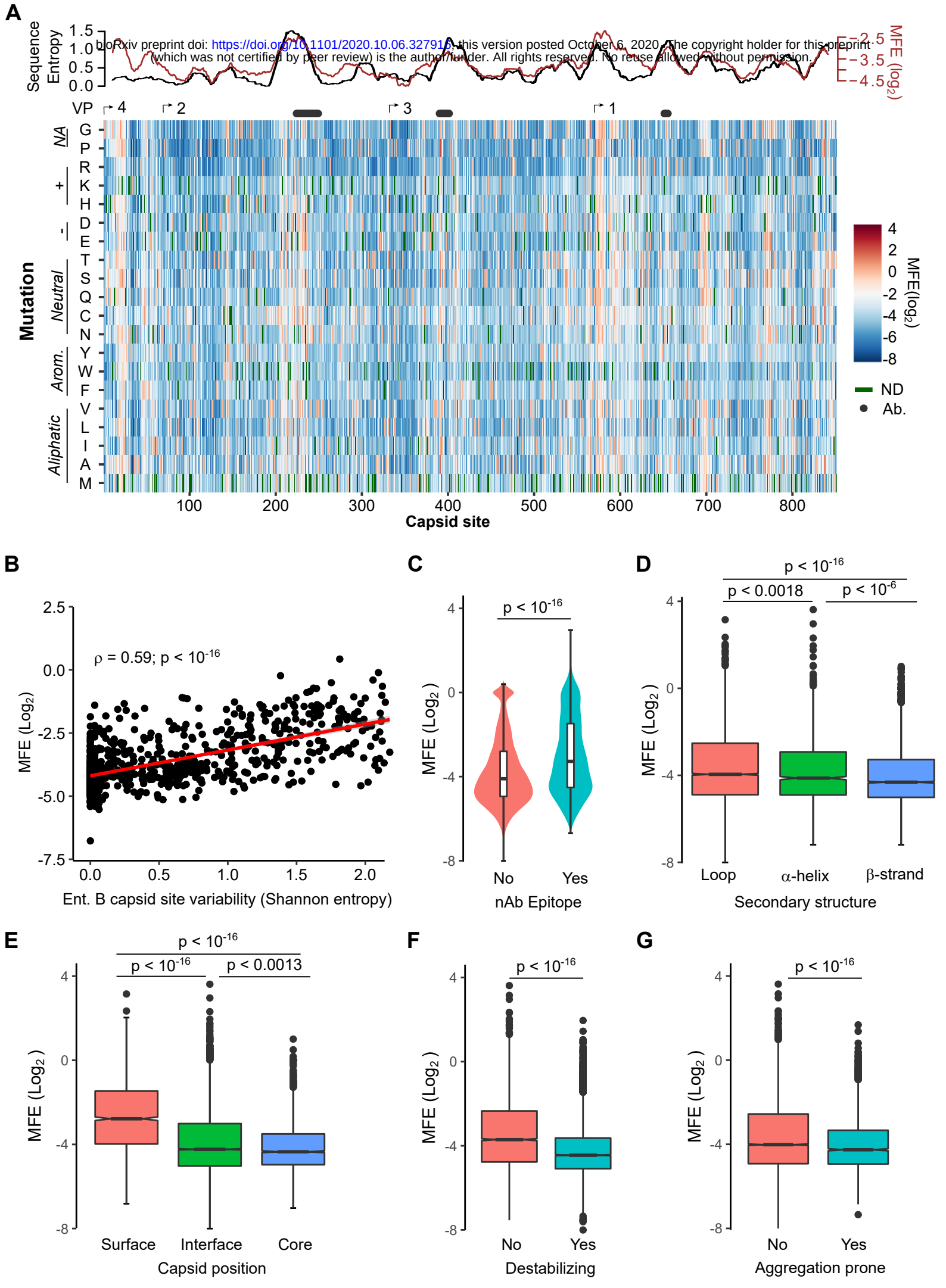

Figure 3. Mattenberger et al.

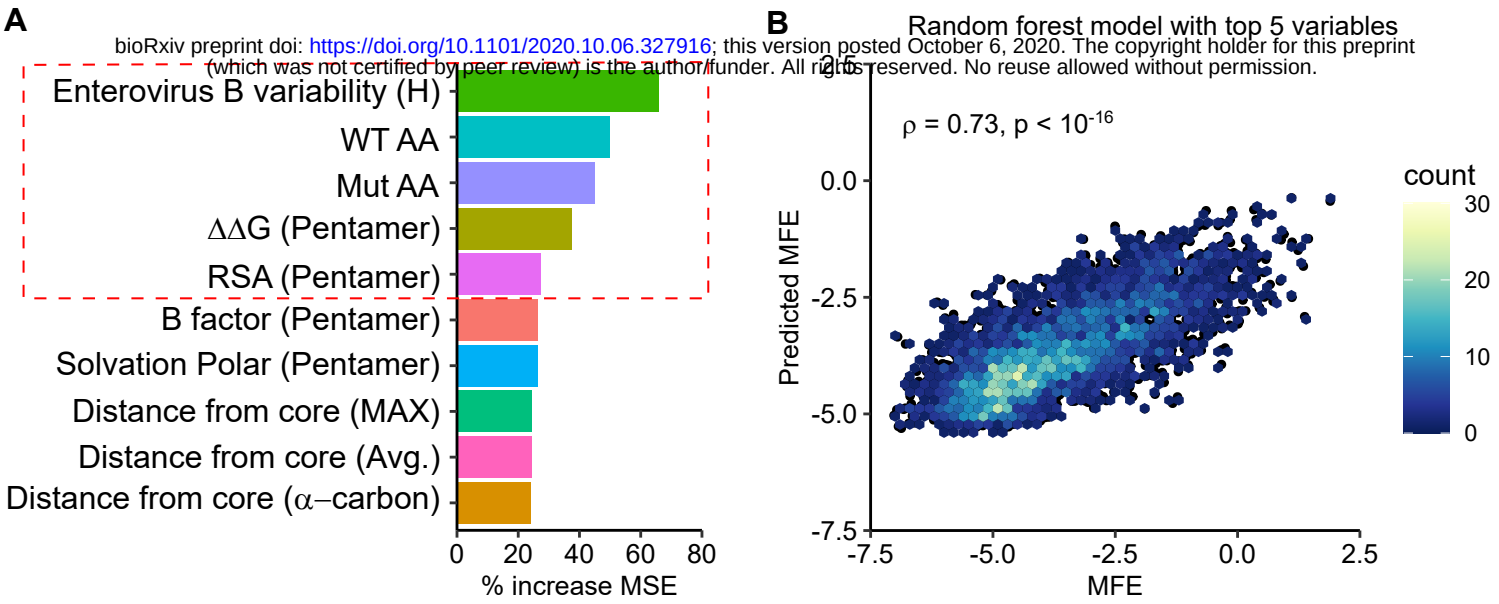

Figure 4. Mattenberger et al.

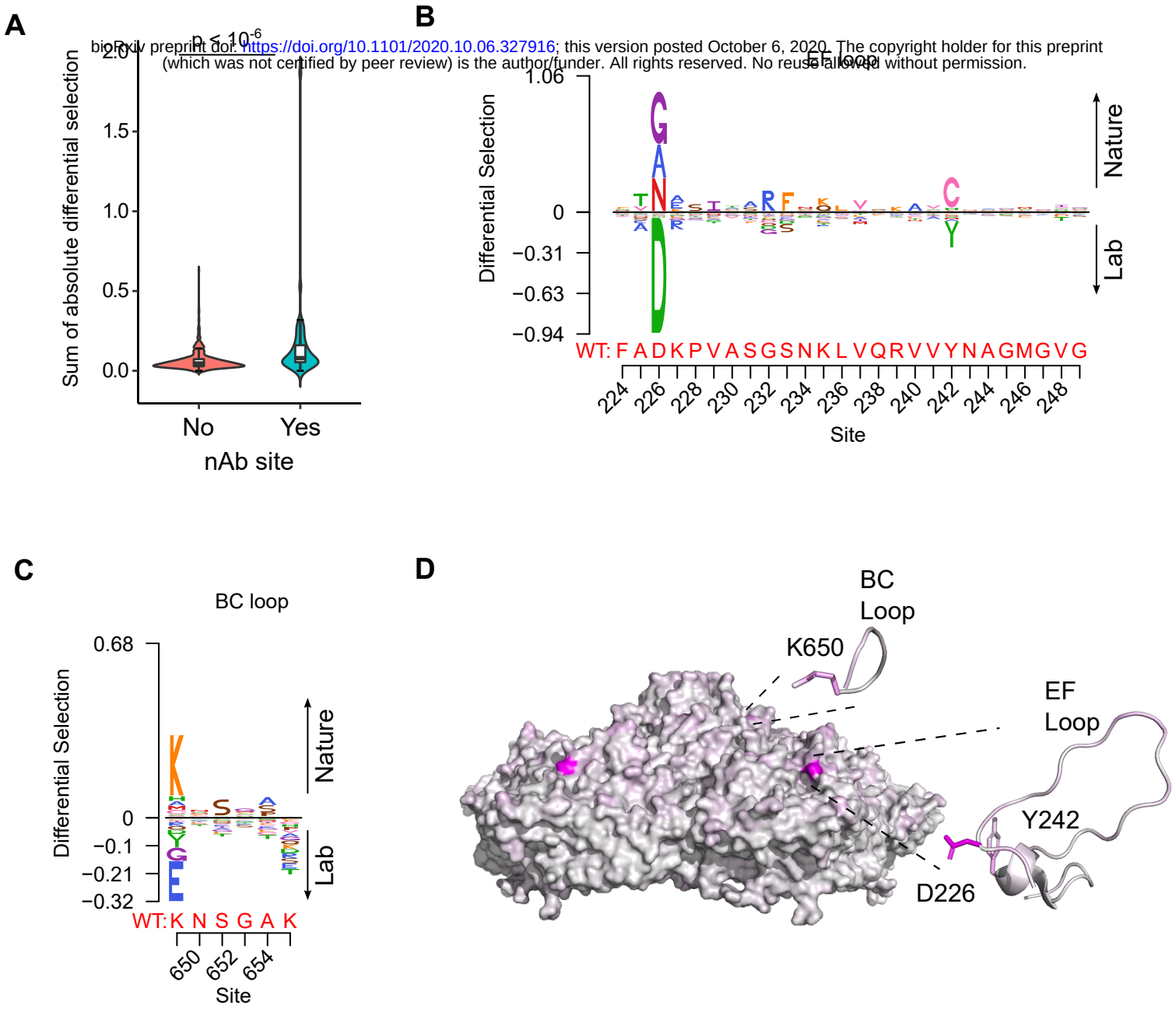

Figure 5. Mattenberger et al.

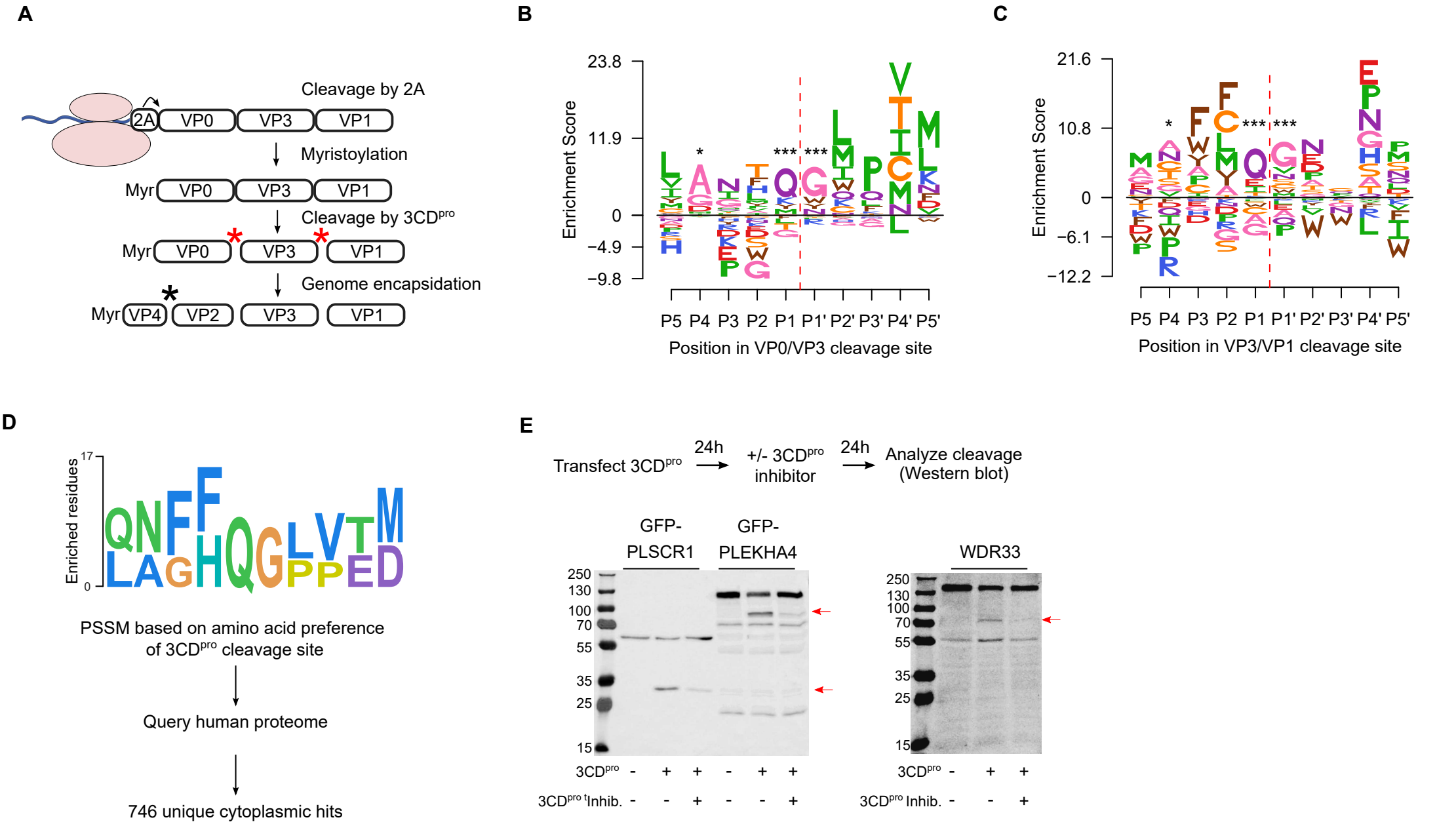

Figure S1. Mattenberger et al.

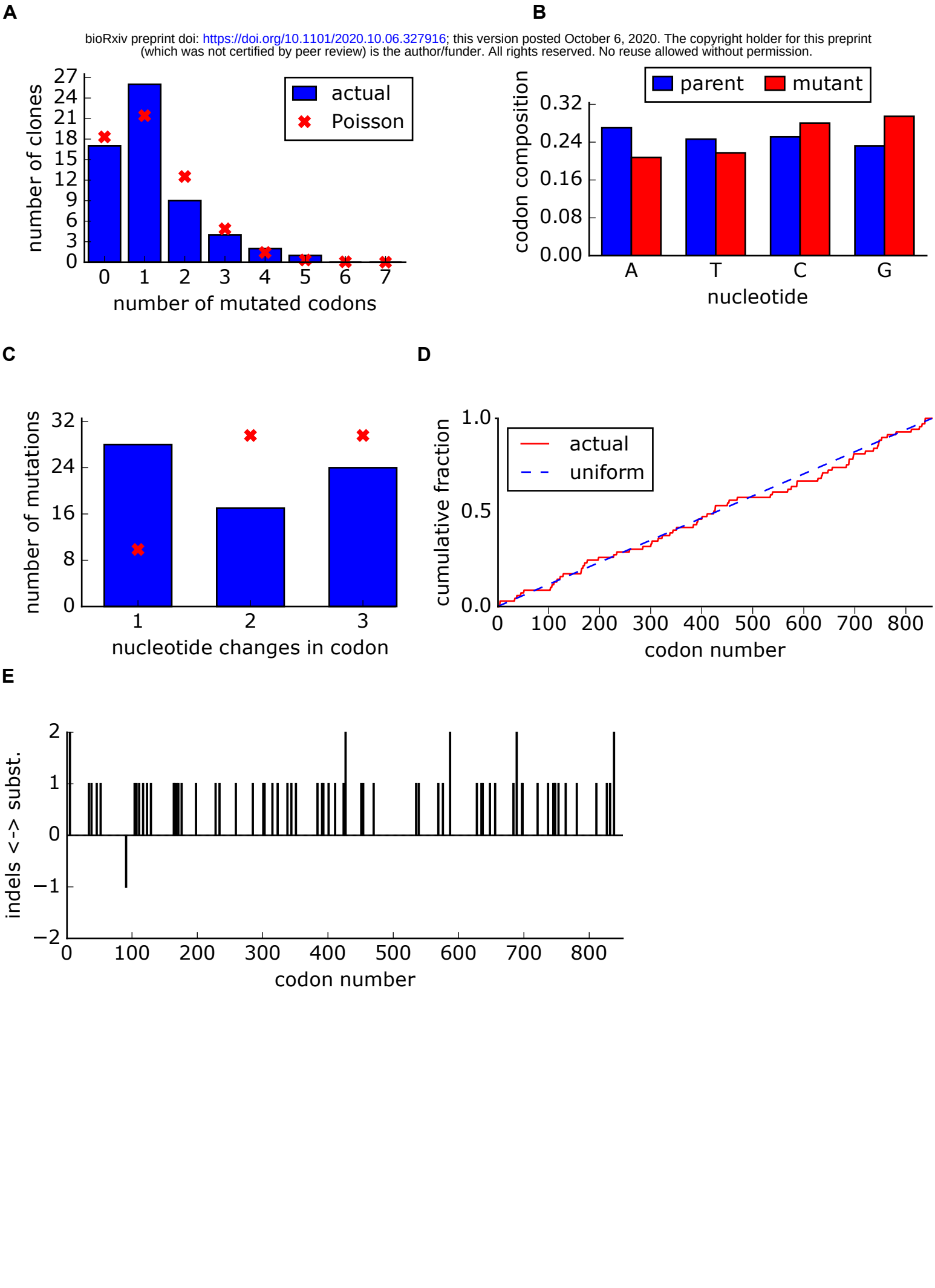

Figure S2. Mattenberger et al.

A

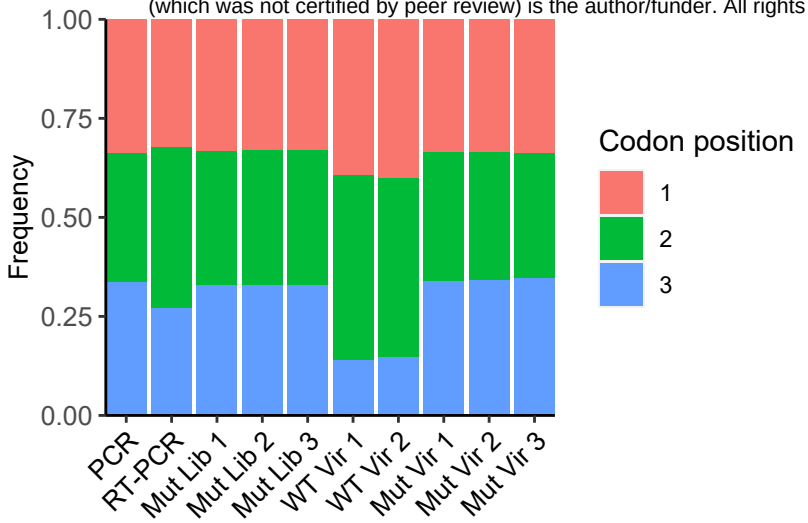

B

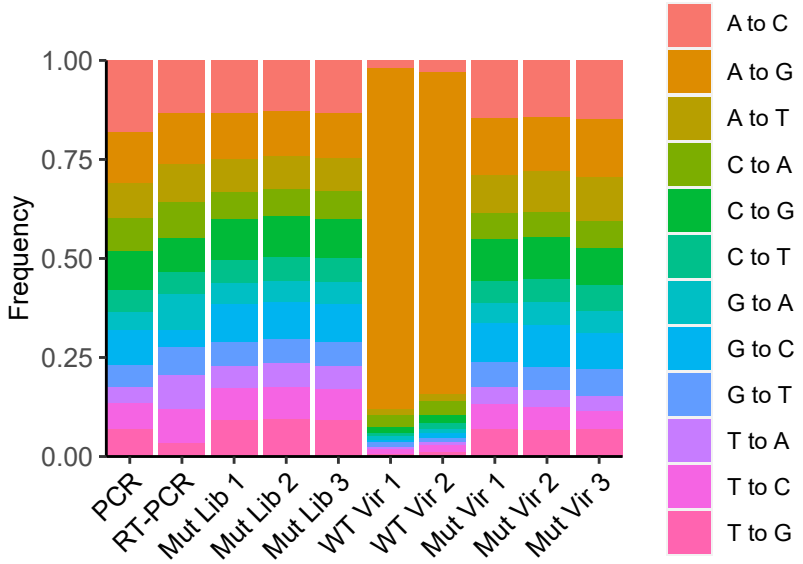

Figure S2. Mattenberger et al.

A

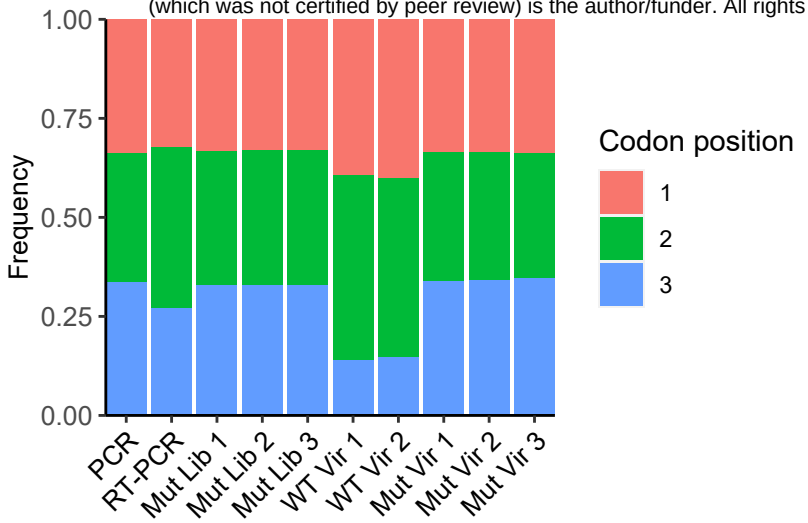

B

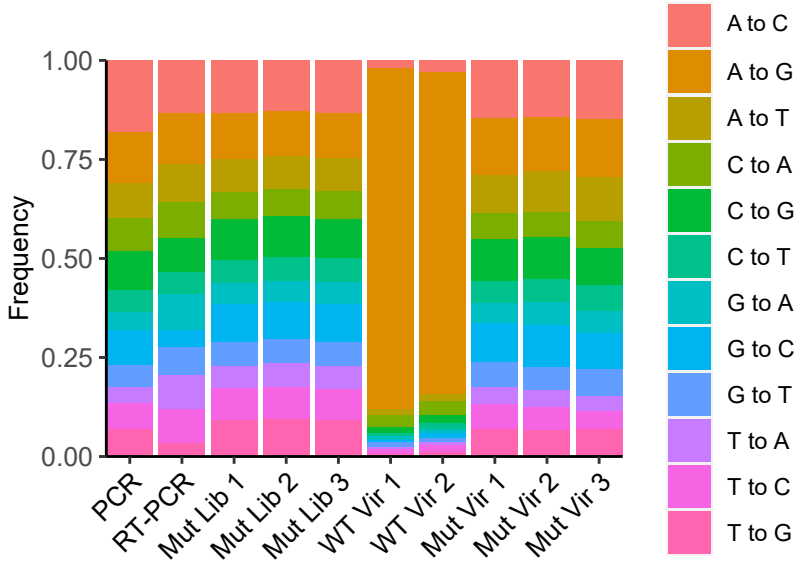

Figure S4. Mattenberger et al.

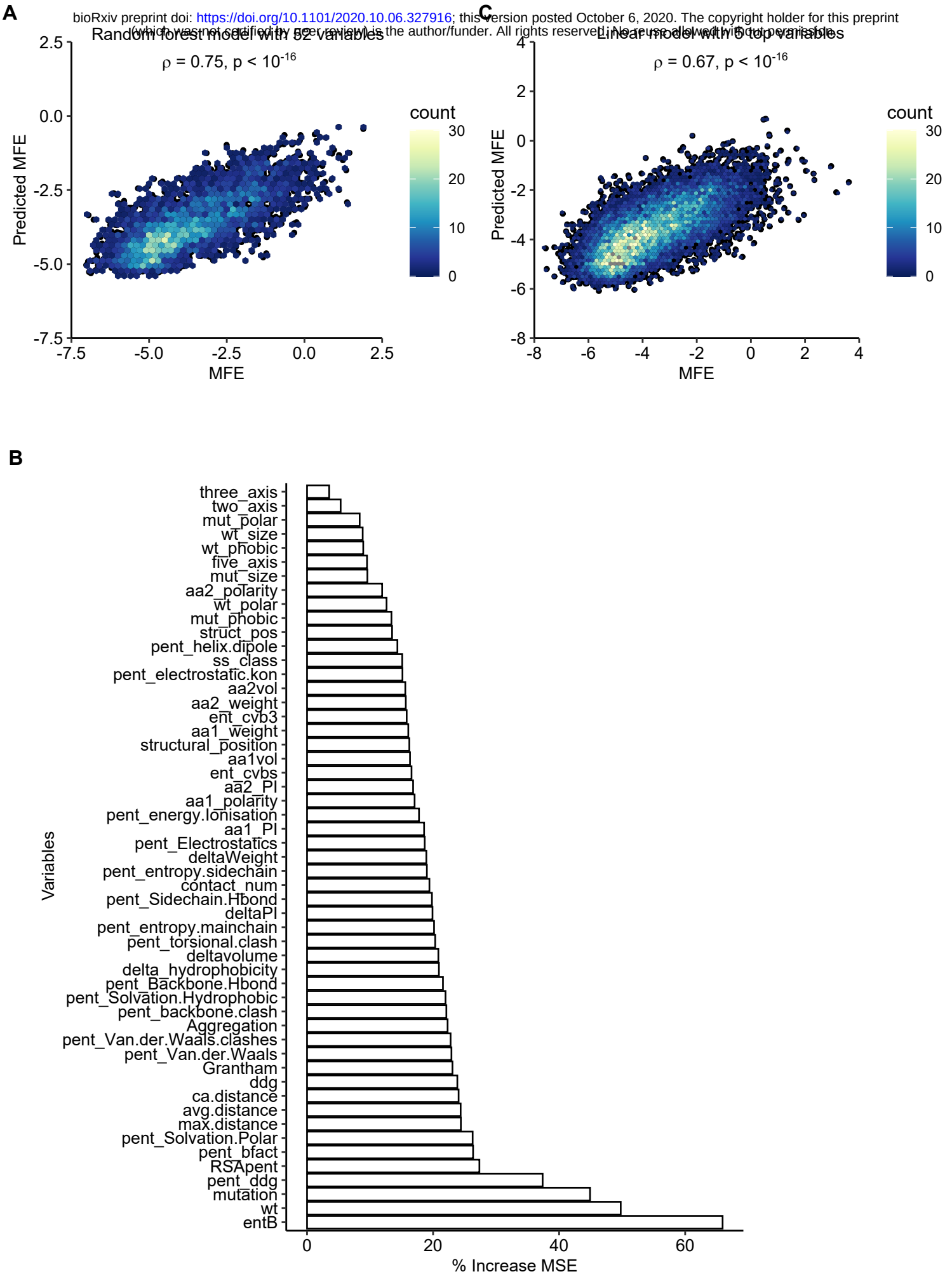

Figure S5. Mattenberger et al.